NUMERICAL INVESTIGATION ON THE EFFECT OF REYNOLDS NUMBER ON TANDEM DROPLET

Shu-Ting Peng[1,2], Fu-Zhen Chen[1,2], Hong Yan[1,2] & Xiao-Qiang Sun[1,2]

[1]School of Power and Energy, Northwestern Polytechnical University, Xi' an, Shannxi, 710072, China
[2]Yangtze River Delta Research Institute of NPU, Northwestern Polytechnical University, Taicang, Jiangsu, 215400, China

Abstract

In aircraft engines, droplets often occur in the form of droplet clusters and directly affect the aerodynamic performance of the engine through gas-liquid interactions. In order to gain a deeper understanding of the dynamic behaviour of dense droplets in airflow, the fluid volume and large eddy simulation methods are employed to perform simulations of the deformation of tandem droplet in continuous airflow and the method has passed the verification of grid independence and numerical validity. The results indicate that the Reynolds number dominates the initial deformation speed of droplets. As the Reynolds number increases, the time required for leading droplet to reach the disk-like structure decreases, while the growth rate of the downstream droplet's cross-stream diameter increases. Specifically, Reynolds number affects the trailing droplet dynamics by affecting the pressure distribution of the wake generated by leading droplet, higher Reynolds numbers result in higher windward stagnation pressure of trailing droplets. Through quantitative analysis, a time evolution function is built to predict the ratio of leading and trailing droplet cross-stream diameters under different Reynolds number, Weber number and relative distance.

Keywords: droplet dynamics; tandem droplet; interaction; Reynolds number; numerical simulation

1. Introduction

In aircraft propulsion systems, the presence of droplets has a profound effect on engine performance. Droplets span several characteristic scales, including millimetre-sized rain droplets ingested by the intake duct and compressor, and micrometre-sized fuel droplets generated by atomizer in the combustor. The differences in scale lead to different Reynolds numbers (Re) of droplet deformation and break-up. In previous studies, a large number of experimental and numerical simulations have been performed to investigate the effects of Weber number (We), Ohnesorge number (Oh) and gas-liquid density ratio (ρ^*) on droplet dynamics. They found that the We number is the main factor determining the droplet breakup mode, while the Oh number affects the critical Weber number (We_{cr}) for droplet breakup mode conversion, and many breakup models have been formulated. In addition, some numerical simulation investigations have found that number also affects the dynamic behaviour of droplets, and an increase in Re number plays a role in promoting droplet deformation to a certain extent, but due to the limitations of experimental methods, it was difficult to clearly capture small-scale fluids to achieve research on low Re number (<1000) droplet deformation or fragmentation.

In aircraft engines, droplets often form clusters. Due to their close relative positions, the dynamic behaviour of different droplets under the influence of the airflow will influence each other, which has been confirmed in some studies. A typical case of tandem droplets has been studied by many researchers. Kumari[1] found that the drag coefficients (Cd) of two droplets in tandem are greater than the Cd of a single droplet under the same conditions. Watanabe[2] carried out numerical simulations of the coalescence and breakup between rising droplets in tandem. The results showed that when two droplets rise vertically at a certain relative distance, coalescence occurs. If the We number at the time of coalescence exceeds We_{cr} number, the coalesced droplet will continue to breakup. Quan[3]

studied the unsteady interaction between droplets under uniform airflow. The results showed that the trailing droplet was significantly affected by the leading droplet, especially for high We numbers and closer distances, where the Cd decreased significantly while the Cd of the upstream droplet decreased slightly. The reason for this is that a high pressure air film forms between the droplets when they are close together. Stefanitsis[4] discovered a 'shuttlecock' type drcoplet breakup mode, where the We_{cr} and breakup time are larger, the Cd and maximum surface area of the trailing droplet are smaller, respectively, compared to the leading droplet.

Due to the multi-scale nature of droplets in aircraft engines, the mechanism of mutual influence between droplets of different Re numbers is still unclear and has not been thoroughly investigated in previous studies. On the other hand, previous studies on the dynamics of dense droplets have focused on low Re numbers and the highest Re number in numerical simulation research is 860 (Stefanitsis et al [4]) up to now, so there is an urgent need to study conditions with higher Re numbers to be applicable to real aviation engine environments. As the Re number increases, the turbulent wake generated by droplets has a more complex impact on the interaction between droplets. In order to further study the mechanism of double droplet interaction, present work numerically simulates the deformation process of two droplets arranged in the streamwise at different relative distances (S: 4-8), Reynolds numbers (Re: 150-1500), and Weber numbers (We: 30-60).

2. Numerical method

2.1 Governing equations

The numerical simulations involved in present work were conducted on the open-source software Basilisk developed by Popinet et al [5]. The Piecewise Linear Interface Capturing (PLIC) VOF method is adopted to represents the free-surface and the conservation of mass and momentum is expressed by the incompressible Navier-Stokes equations with surface tension:

$$\rho(\partial_t u + u \cdot \bigtriangledown u) = -\bigtriangledown p + \bigtriangledown \cdot (2\mu D) + f_\sigma \tag{1}$$

$$\partial_t \rho + \bigtriangledown \cdot (\rho u) = 0 \tag{2}$$

$$\bigtriangledown \cdot u = 0 \tag{3}$$

where $D = [\bigtriangledown u + (\bigtriangledown u)^T]/2$ represents the deformation tensor, and $\rho = \rho_g + c(\rho_l - \rho_g)$, u, p, $\mu = \mu_g + c(\mu_l - \mu_g)$ respectively represent dynamic density, velocity, pressure, and dynamic viscosity of the flow field. The last term on the right-hand in equation (1) is surface tension force, which is modeled as volumetric force using the continuum surface force (CSF) method:

$$f_\sigma = \sigma k \delta_s n \tag{4}$$

where the surface tension coefficient σ considered constant, k, δ_s, n respectively represent the curvature of interface, Dirac function, and interface normal.

The solution of the governing equations utilizes the approximate projection method to solve the coupling of (1) and (3), and the method of multigrid cycle to accelerate the solving of the Poisson equation, thereby obtaining an approximately divergence-free velocity field. The velocity and momentum are calculated using a second-order upwind Bell, Colella and Glaz (BCG) scheme, while the diffusion flux due to the viscous term is solved using a semi-implicit Crane-Nicholson scheme.

2.2 LES formulation

In the present work, due to the high Re number (up to 1500), using DNS for complete resolution of turbulence dissipation requires significant computational resources. So the Dynamic Smagorinsky model Proposed by Lilly [6] is used here to close the sub-grid stress term.

The current two-phase LES governing equations is represented as the filtered conservation of mass and momentum equation:

$$\frac{\partial \bar{u}_i}{\partial x_i} = 0 \tag{5}$$

$$\frac{\partial \bar{u}_i}{\partial t} + \frac{\partial \bar{u}_i \partial \bar{u}_j}{\partial x_j} = -\frac{1}{\rho}\frac{\partial \bar{p}}{\partial x_i} + \frac{1}{\rho}\frac{\partial \bar{\tau}_{ij}}{\partial x_j} + \frac{1}{\rho} f_{\sigma k} \tag{6}$$

where superscript "−" represents the main filter while superscript "∧" represents the test filter. By solving the SGS stress tensor, we obtain the eddy viscosity coefficient:

$$\bar{\tau}_{ij} = 2\mu_t \bar{S}_{ij} = 2(\mu + \mu_{SGS})^{1/2} \tag{7}$$

$$\mu_{SGS} = \rho C_s (\Delta_1)^2 (2\bar{S}_{ij}\bar{S}_{ij})^{1/2} \tag{8}$$

$$\bar{S}_{ij} = \frac{1}{2}(\frac{\partial \bar{u}_i}{\partial x_j} + \frac{\partial \bar{u}_j}{\partial x_i}) \tag{9}$$

Introducing local structural information of end flow into sub-grid through two rounds of filtering and dynamically determining model coefficients C_s during the calculation process. The main filter width is (take as the cube root of the local cell volume), and the test filter width is $\Delta_2 = 2\Delta_1$:

$$C_s = \frac{1}{2}(\frac{L_i j M_{ij}}{M_{ij}^2}) \tag{10}$$

where

$$M_{ij} = \Delta_2^2 \left|\bar{S}\right| \bar{S}_{ij} - \Delta_1^2 \widehat{\left|\bar{S}\right| \bar{S}_{ij}} \tag{11}$$

3. Results and discussion

3.1 Computational setup and verification

To date, a large number of numerical investigations about droplet deformation and breakup have been achieved using adaptive mesh refinement techniques. However, there have been few previous studies on the testing of gas phase resolution for droplet deformation and breakup, and it is still unclear whether the turbulent wake structure generated by the leading droplet will affect the deformation morphology of droplet. It is necessary to verify the convergence of the grid, so four different meshes were used to test the independence of the grid.

This test was carried out in a $16D * 16D$ computational domain, with a droplet placed at a distance of $4D$ from the left face. The left boundary condition assumes a velocity inlet with null pressure gradient while the right face is set as the outflow condition with fixed pressure $p = 0$ and null velocity gradient. The other faces are set as free-slip boundary conditions. Due to the explicit discretisation of the surface tension term, the setting of the time step should strictly follow the numerical stability conditions to avoid stability issues related to surface tension. Therefore, with reference to the numerical stability conditions proposed by Galusinski et al [7], the time step size is set as follows:

$$\Delta t \leq min(\Delta t_c, \Delta t_{STK}) = min(\sqrt{\frac{\rho_g}{\sigma}\Delta x_{min}^3}, \frac{\mu_g}{\sigma}\Delta x_{min}) \tag{12}$$

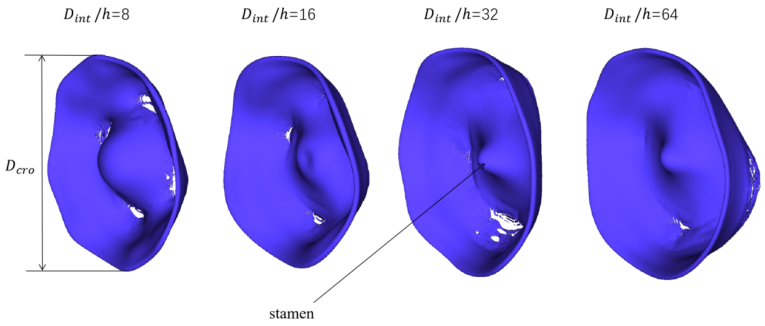

Figure 1 – Gas-liquid interface at different resolutions.

The gas-liquid interface at $T = 1.8125$ for We number 30 and Re number 1500 is shown in Figure 1 and the droplet presents a bag-stamen breakup mode. Different resolutions are used to refine the pure gas/liquid phase, and the phase interface resolution is set to $D_{int}/h = 64$, here h is the minimum grid scale. As the gas-phase resolution increases, the stamens of the droplets become sharper and the cross-stream diameter (D_{cro}) of the droplet slightly increases and this result also

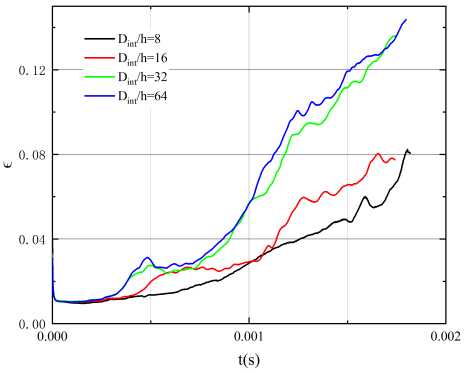

Figure 2 – Gas-phase dissipation rate at different resolutions.

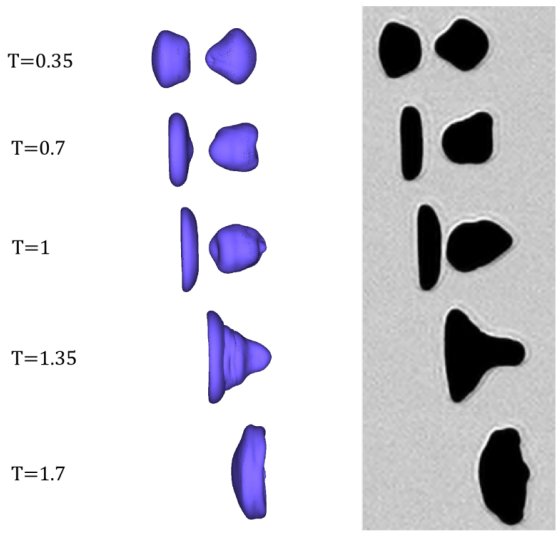

Figure 3 – Comparison between simulation and experimental (Wang et al [5]).

indirectly suggests the influence of small-scale turbulence on the deformation process of droplets. For case of $D_{int}/h = 32$ and $D_{int}/h = 64$, the droplet showed similar shapes. Figure 2 shows the gas phase turbulence dissipation rate ε under four different meshes. As the resolution increases, the turbulence dissipation rate increases, indicating that low resolution meshes underestimate the turbulence dissipation rate. In order to save computational resources, the minimum grid scale for the pure gas/liquid zone $D_{int}/h = 32$ was selected to complete the subsequent simulation work.

To validate the numerical method, a comparison was made between the experimental results of Wang [8] and the numerical simulation results. The comparative operating conditions are $S = 2.1$, $Re = 2500$, and $Oh = 0.0024$. The Re number used for comparison is higher than the cases involved in present work, however, but the results (Figure 3) still show good consistency. Therefore, it can be demonstrated that the numerical method used in present work can effectively simulate the deformation process of tandem droplet.

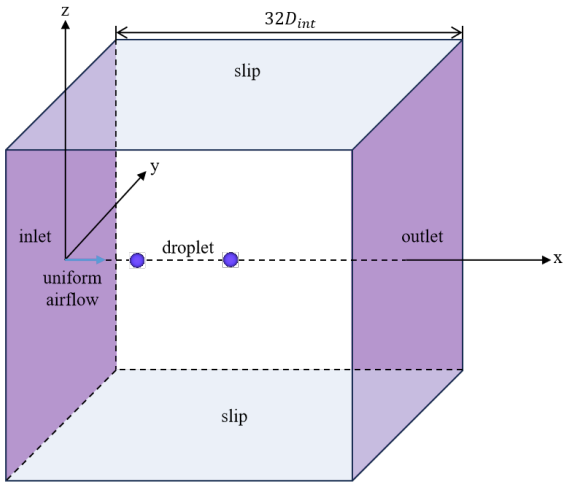

Figure 4 – Computational domain and boundary conditions.

To simulate the deformation process of tandem droplet, the computational domain is set as follows. The overall setting is similar to the previous work, with the width of the domain set to $32D$ and the distance between the leading droplet and the left face is $8D$, as shown in Figure 4. The density ratio $\rho^* = \rho_l/\rho_g = 1000$ and viscosity ratio $\mu^* = \mu_l/\mu_g = 122.27$ are chosen and we employ adaptive

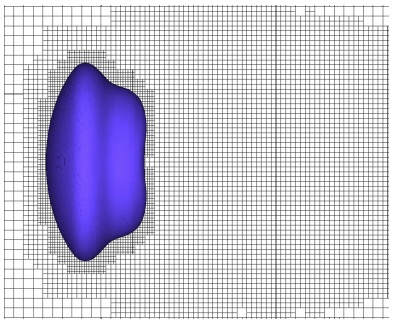

Figure 5 – Adaptive mesh refinement of field.

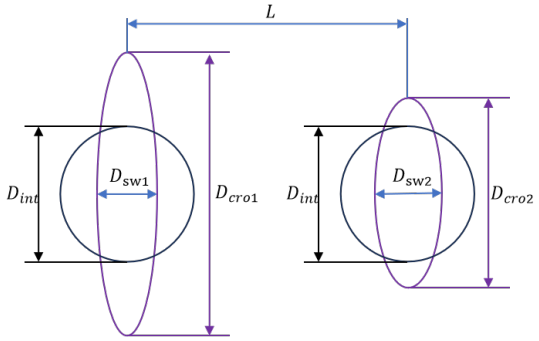

Figure 6 – Droplet shape parameters.

mesh refinement using a cost function based on volume fraction, velocity, and local velocity gradient, ensuring the capture of small-scale turbulent structures (Figure 5). The highest resolution near the free-surface $(0 < c < 1)$ is set to $D_{int}/h = 64$ while for pure gas/liquid phase, it is set to $D_{int}/h = 32$. For the convenience of further discussion, the definition of the droplet shape parameters is shown in Figure 6 and the calculated cases are shown in Table 1.

Table 1 – Non-dimensional numbers involved in present work

$D = \frac{L}{D_{int}}$	$Re = \frac{\rho_g D_{int} U}{\mu_g}$	$We = \frac{\rho_g D_{int} U^2}{\sigma}$
4	150	30
4	750	30
4	750	45
4	750	60
6	750	30
8	150	30
8	150	45
8	150	60
8	300	30
8	300	45
8	300	60
8	750	30
8	750	45
8	750	60
8	1500	30
8	1500	60

3.2 Leading droplet

The numerical simulation results show that there are differences in the dynamic behavior of leading droplet at different Re numbers, consistent with Feng's [9] research findings. Due to the stronger advection effect of the droplet wake at high Reynolds numbers, resulting in the formation of complex vortex structures on the leeward side (Figure 11) and leads to a sharper droplet shape which can be seen in Figure 7. Due to the pressure difference between the windward and leeward sides of the droplets, liquid move towards the leeward side (Figure 11). A strong momentum exchange occurred between the vortex and the liquid, causing the liquid on the leeward side to move in the opposite direction of flow, eventually converging with the windward liquid at the red chain line along the way, and then flowing towards the cross flow direction, causing the liquid droplet to flatten. It can be seen that the red chain line is not located at the equatorial position of the droplet. By analyzing the surface pressure of droplets on the windward and leeward surfaces, it was found that both the pressure surface forces on the windward and leeward surfaces tend to force the droplets in the streamwise of

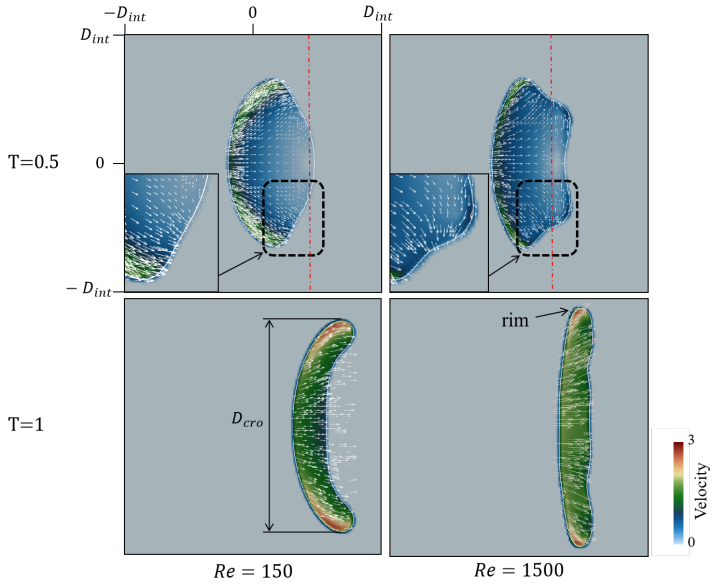

Figure 7 – Velocity contour of leading droplet for $We = 30$.

flow (Figure 8). This explains the phenomenon founded by Jackiw [10] and Flock [11], which states that during the deformation process, droplet do not deforms symmetrically about its equator until it forms a uniformly flattened disk shape.

For low Reynolds number cases, the shape of the droplet is more smooth. It can be seen that for the condition of $Re = 150$, the periphery of the droplet has a greater flow velocity, and the convergence position of the droplets (marked with red chain line) is closer to the leeward side than $Re = 1500$. This leads to a slower rate of flattening of the droplet.

By integrating droplet along the surface, the trend of droplet pressure drag (F_p) and viscous drag (F_μ) over times can be obtained:

$$F_{drag} = F_\mu + F_p = \int_A \mathbf{n} \cdot \mathbf{S} \cdot \mathbf{i} dA + \int_A -p\mathbf{n} \cdot \mathbf{i} dA \tag{13}$$

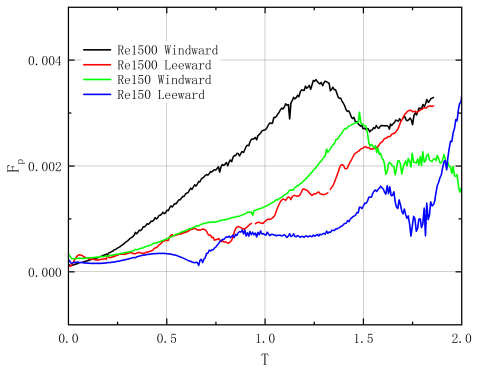

Figure 8 – Pressure surface force on the windward and leeward surfaces of leading droplet for $We = 30$.

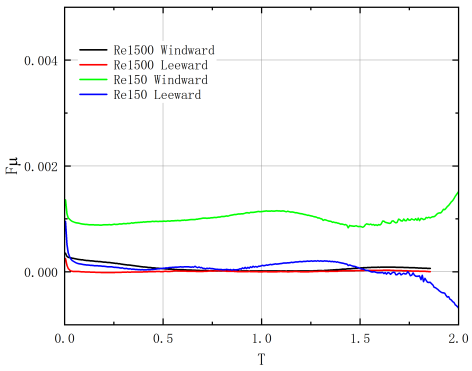

Figure 9 – Viscosity surface force on the windward and leeward surfaces of leading droplet for $We = 30$.

We compared the pressure drag and viscous drag on the windward and leeward surfaces of droplets at different Reynolds numbers and observed significant differences (Figure 8 & Figure 9). When $Re = 1500$, both the windward and leeward sides of the droplet are subjected to greater pressure surface forces compared to $Re = 150$ due to the larger windward area and lower liquid velocity at the periphery. A lower periphery velocity leads to a higher relative gas-liquid velocity and ultimately

resulting in a higher stagnation pressure. At high Reynolds numbers, the viscous drag contribution is almost non-existent, while at low Reynolds numbers the viscous drag increases and is mainly contributed by the windward surface. When the liquid bag begins to form, the liquid accelerates rapidly resulting the stagnation pressure on the windward side decreases. Therefore, we can observe a rapid decrease in the pressure drag on the windward side in Figure 8.

As a key structure for distinguishing between droplet deformation and fragmentation, the spatio-temporal parameters of the disk-like structure deserve in-depth investigation. The study of the initial deformation process from spherical to disk-like structure is crucial to accurate construction of a secondary fragmentation model. According to the analysis results in the previous section, it can be seen that the Re number has a significant effect on the internal flow of droplets, affecting the relative motion state of the liquid at the periphery and the centre of the droplet. Based on this viewpoint, Kékesi [12] derived a theoretical model for predicting the droplet breakup mode, which can effectively predict the droplet breakup mode at low Re numbers. However, this relationship is only applicable to low Re number operating conditions, so studying the initial deformation time (T_{int}) of droplet in a wider range of Re numbers has great reference value for improving this model and revealing the dynamic mechanism of droplet deformation. We compared the time for the droplets to reach the disk-like structure under

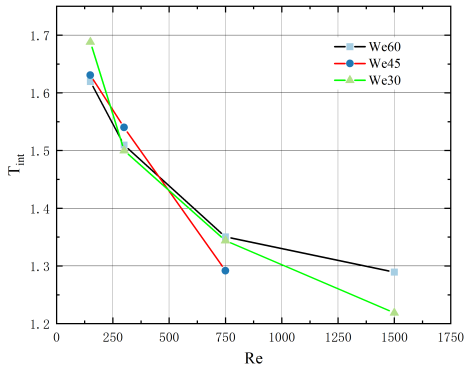

Figure 10 – Initial deformation time of leading droplet at different Reynolds numbers.

different We numbers and Re numbers, similar to previous research (Jackiw et al. [10]), the moment when the minimum flow diameter D_{sw1} occurs is defined as the moment when fragmentation begins, which is the moment when the droplet appears as a disk-like structure. The results (Figure 10) show that as the Re number increases, the initial deformation time for droplets to reach the disk-like structure decreases, and the relationship with We number is not obvious, i.e. the Reynolds number is the main factor dominating the droplet deformation speed. Finally, we obtain the relative relationship between T_{int} and the Re number by data fitting:

$$T_{int} = 1.24 + 0.6e^{-\frac{Re}{390}} \tag{14}$$

3.3 Trailing droplet

The difference in Re number not only causes differences in the morphology of the leading droplet, but also has a significant effect on the trailing droplet. As shown in Figure 11, the evolution of the morphology of the droplet interfaces under different Re numbers is listed. Except for the Re number 150, both leading and trailing droplets show a similar mode, both in a bag-stamen mode. However, at $Re = 150$, the trailing droplet becomes disk-like with no evidence of stamen formation. At low Re numbers, the droplet shape is smoother; as the Re number increases, the droplet stamen structure begin to become sharp,and the cross-flow diameter of the droplet slightly increases while the R-T wave number at the droplet rim are more pronounced.

Based on the dimensionless time defined by Nicholls [13] ($T = \frac{D_{int}\sqrt{\rho^*}}{U}$), the droplet shape and pressure distribution at different times ($T = 0.5, 1, 1.5$) was plotted (Figure 12). It can be observed that as the Re number increases, the pressure of the wake generated by the leading droplet decreases.

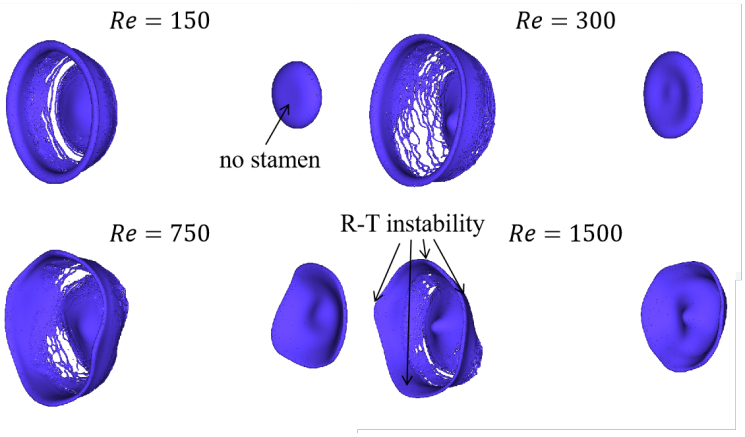

Figure 11 – Droplet breakup at different Reynolds numbers for $We = 30$.

When the Re number is 150, the leading droplet wake vortex sheds and two symmetrical low-pressure regions are formed at the droplet tail. As the Re number increases to 300, the tail vortex of the droplet undergoes asymmetric shedding, and it can be seen that due to the asymmetric shedding of the tail vortex, the pressure distribution on the leeward side of the droplet is uneven, ultimately leading to the rotation of the droplet. As the Re number of droplet increases, the droplet wake vortex begins to shed randomly, forming a turbulent wake region. For trailing droplet, its deformation is more suppressed

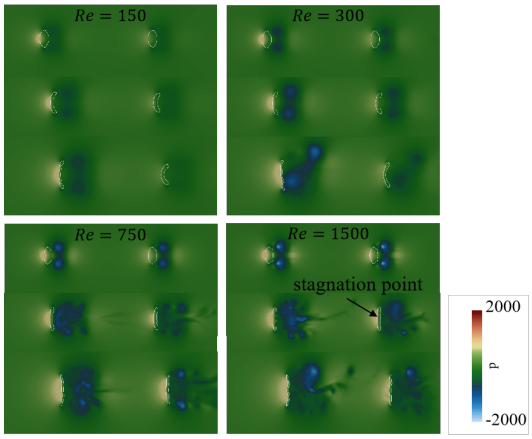

Figure 12 – Tandem droplet morphology and pressure contour at different Reynolds numbers for $We = 30$.

at low Re numbers. The pressure distribution shows that high Re numbers result in higher pressure at the windward stagnation point of the trailing droplet. Due to the increased pressure difference between the stagnation point on the windward side of the droplet and the leeward side of the droplet, the droplet is subjected to a stronger “squeezing” effect. Therefore, trailing droplet is more likely to develop into liquid bags at high Re numbers. When the leading droplet has a disk-like structure, we performed statistic on the ratio of the cross-stream diameter (D_r) of the leading and trailing droplets at different relative positions (S). The cross-stream diameter of the droplet is calculated from the projected area of the droplet:

$$D_r = \frac{D_{cro1}}{D_{cro2}} = \frac{\sqrt{\frac{A_{pro1}}{\pi}}}{\sqrt{\frac{A_{pro2}}{\pi}}} \tag{15}$$

We found that when the leading droplet has a disk-like structure for the same Re number, the ratio of the cross-stream diameters between the leading and trailing droplets at different We numbers or different relative distances does not differ much. Except for the influence of S and D_r, just increases slightly with increasing number (Figure 13). According to the previous findings, the time that the droplet spends to reaches the disk-like structure is also dominated by the Re number. Therefore,

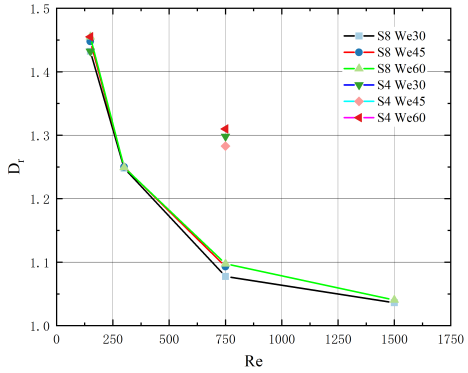

Figure 13 – Cross-stream diameter ratio between two droplets while the leading droplets show a disk-like structure.

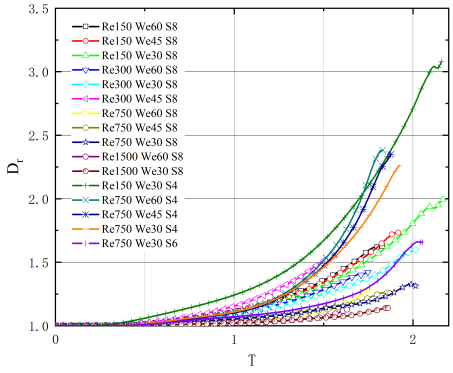

Figure 14 – The temporal evolution relationship of D_r.

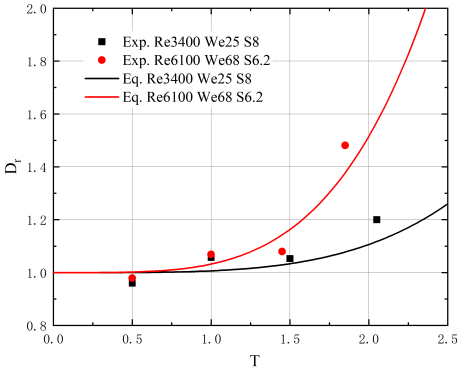

Figure 15 – Comparison between Equation (16) and experimental results (Wang et al. [8]).

we speculate that as the droplets deform, the ratio of the leading and trailing droplet cross-stream diameters should also be determined by the Re number, with small correlation with the We number. We quantitatively analysed all the calculated cases in the present work and obtained the relationship between D_r and non-dimensional time T as shown in Figure 14. The time experienced is the entire deformation stage of the leading droplet, i.e. until the droplet fragments (the free-surface of the droplet initially appears with holes or sub-droplets peel off from the parent droplet). The results confirmed our hypothesis: the ratio of the cross-stream diameter of the leading and trailing droplets D_r is mainly determined by the Re number at the same relative distance. At the same time, it can be seen that at relatively short distance ($S = 4$), the increases faster over time than longer distance ($S = 8$). This is because as the S decreases, the stagnation point pressure of trailing droplets on the windward surface decreases, resulting in a lower pressure difference between the windward and leeward surfaces. As the We number increases, the growth rate of D_r increases slightly over time because the leading droplet cross-stream diameter (D_{cro}) becomes larger as We number increases which has been confirmed in many investigations.
The time evolution correlation of D_r obtained by data fitting is as follows:

$$D_r = 1 + 0.48T^4 e^{-\frac{S}{AB}} \tag{16}$$

Where A and B represent the influence of Re number and We number, $A = (1.97 + 2.1e^{-\frac{Re}{505}})$, $B = (1.2 - 0.8e^{-\frac{We}{21.64}})$. The comparison with Wang's [8] experimental results shows that the correlation function pridicts the deformation process of tandem droplet well (Figure 15).

4. Conclusion

In the present study, the deformation of tandem droplet in continuous airflow was investigated numerically. The droplet deformation process was calculated for different Reynolds numbers (150-1500) in different scale droplet environments in aircraft engines. The simulation results indicate that for isolated droplets, due to the pressure gradient between the windward and leeward surfaces and asymmetric internal flow, they do not symmetrically deform from spherical to disk-shaped along the equatorial position. The pressure surface forces on both the windward and leeward surfaces drag the droplets in the direction of airflow. With the increase of Reynolds number, complex secondary vortex structures are formed behind the leeward surface of the droplets and the cross-stream diameter expansion speed is faster which leading to the formation of a flatter and wider windward surface, resulting in an increase in pressure surface forces eventually. The degree of influence on trailing droplet varies for different Reynolds numbers. Specifically, as the Reynolds number decreases, the growth rate of the ratio of leading and trailing cross-stream diameter D_r increases . In addition, as We increases or S decreases , the degree of inhibition on droplets also slightly increases. A function was proposed to describe the variation of D_r with non-dimensional time T at different We numbers, Re numbers, and relative distances S by data fitting. This function provides a reference for predicting the drag of droplets under Lagrangian description for modeling the evolution process of droplet velocity over time in dense droplet fields more accurate.

5. Contact Author Email Address

Shu-Ting Peng
Email: 760144254@qq.com

6. Acknowledgment

The research is conducted under the sponsorship from the General Program of the National Natural Science Foundation of China(No. 12272321), the Science and Technology Plan Project of Taicang City(No. TC2022JC10), the Key Research and Development Plan Project of Shanxi Province(No. 2022SF-151).

7. Copyright Statement

References

[1] Kumari N, Abraham J. Interactions of decelerating drops moving in tandem. *Atomization & Sprays*, Vol. 18, No. 3, pp 191-241, 2008.

[2] Watanabe T, Ebihara K. Numerical simulation of coalescence and breakup of rising droplets. *Computers & Fluids*, Vol. 32, No. 6, pp 823-834, 2003.

[3] Quan S, Lou J, Stone H A. Numerical investigation of the aerodynamic breakup of a parallel moving droplet cluster. *Journal of Fluid Mechanics*, Vol. 684, pp 103123-103123, 2011.

[4] Stefanitsis D, Malgarinos L. Numerical investigation of the aerodynamic breakup of a parallel moving droplet cluster. *International Journal of Multiphase Flow*, Vol. 121, No. C, pp 103123-103123, 2019.

[5] Popinet, Stéphane. A quadtree-adaptive multigrid solver for the Serre–Green–Naghdi equations. *Journal of Computational Physics*, Vol. 302, pp 336–358, 2019.

[6] Lilly D K. A proposed modification of the Germano subgrid-scale closure method. *Physics of Fluids*, 1991.

[7] Galusinski C, Vigneaux P. On stability condition for bifluid flows with surface tension : application to microfluidics. *Journal of Computational Physics*, Vol. 227, No. 12, pp 6140-6164, 2008.

[8] Wang Z, Hopfes T, Giglmaier M. Experimental investigation of shock-induced tandem droplet breakup. *Physics of Fluids*, Vol. 33, No. 1, pp 012113, 2021.

[9] Feng J Q. A deformable liquid drop falling through a quiescent gas at terminal velocity. *Journal of Fluid Mechanics*, Vol. 658, pp 438-462, 2010.

[10] Jackiw I M. On aerodynamic droplet breakup. *Journal of Fluid Mechanics*, Vol. 913, pp A33, 2021.

[11] Flock A K, Guildenbecher D R, Chen J. Experimental statistics of droplet trajectory and air flow during aerodynamic fragmentation of liquid drops. *International Journal of Multiphase Flow*, Vol. 47, pp 37-49, 2019.

[12] Kékesi T, Amberg G. Drop deformation and breakup. *International Journal of Multiphase Flow*, Vol. 6, pp 1-10, 2014.

[13] Nicholls J A, Ranger A A. Aerodynamic shattering of liquid drops. *AIAA Journal*, Vol. 7, No. 2, pp 285-290, 1969.